Biofabrication



RECEIVED

1 December 2019

REVISED

6 March 2020

ACCEPTED FOR PUBLICATION 16 April 2020

PUBLISHED 10 March 2021

PAPER

High throughput direct 3D bioprinting in multiwell plates

Henry H Hwang^{1,5}, Shangting You^{1,5}, Xuanyi Ma², Leilani Kwe¹, Grace Victorine³, Natalie Lawrence¹, Xueyi Wan¹, Haixu Shen¹, Wei Zhu⁴ and Shaochen Chen^{1,2,3}

- Department of NanoEngineering, University of California San Diego, 9500 Gilman Dr, La Jolla, CA 92093, United States of America
- Department of Bioengineering, University of California San Diego, 9500 Gilman Dr, La Jolla, CA 92093, United States of America
- ³ Chemical Engineering Program, University of California San Diego, 9500 Gilman Dr, La Jolla, CA 92093, United States of America
- Allegro 3D, Inc., 6868 Nancy Ridge Drive, San Diego, CA 92121
- ⁵ These authors contributed equally

E-mail: chen168@eng.ucsd.edu

Keywords: 3D printing, tissue engineering, drug screening, high throughput, multiwell plates

Supplementary material for this article is available online

Abstract

Advances in three dimensional (3D) bioprinting have enabled the fabrication of sophisticated 3D tissue scaffolds for biological and medical applications, where high speed, high throughput production in well plates is a critical need. Here, we present an integrated 3D bioprinting platform based on microscale continuous optical printing, capable of high throughput in situ rapid fabrication of complex 3D biomedical samples in multiwell plate formats for subsequent culture and analysis. Our high throughput 3D bioprinter (HT-3DP) was used to showcase constructs of varying spatial geometries of biomimetic significance, tunable mechanical properties, as well as reproducibility. Live hepatocellular carcinoma 3D tissue scaffolds were fabricated in situ in multiwell plates, after which a functional drug response assay against the chemotherapy drug doxorubicin was performed. Dual cell-type populations involving both live hepatocellular carcinoma as well as human umbilical vein endothelial cells were also printed to demonstrate dual-tissue fabrication capability. This work demonstrates a significant advancement in that the production rate of 3D bioprinted tissue scaffolds with controllable spatial architectures and mechanical properties can now be done on a high throughput scale, enabling rapid generation of in vitro 3D tissue models within conventional multiwell cell culture plates for high throughput preclinical drug screening and disease modeling.

1. Introduction

Pharmacological research and development is currently a tedious and failure-prone endeavor, with an approved product taking potentially up to 12-15 years [1] and upwards of \$2.6 billion USD in development costs [2] before making it to market. The failure modes often involve the transition between validation phases of the development pipeline, e.g. hits generated from in vitro screenings failing in pre-clinical animal models [3], or the few successful hits in animal models failing to successfully translate to humans during clinical testing [4]. In this context there is significant interest in using humanorigin in vitro models, specifically three-dimensional (3D) engineered tissue constructs, whose efficacy and potential to approach the complexity of human in vivo systems outstrips that of traditional 2D

monolayer cell culture systems [5–9]. While advances in 3D bioprinting have enabled precise fabrication of engineered tissue scaffolds of varying complexity, low throughput and low reproducibility can limit these technologies' use in applications where large quantities of consistent, functional samples are important, such as the high throughput screening (HTS) methods commonly employed in various biological, chemical, and pharmaceutical domains.

In this work, we present a digital light processing (DLP)-based, rapid continuous 3D-bioprinting platform capable of automated well plate printing, for high throughput *in situ* fabrication of 3D tissue constructs of up to 96 samples per batch. This is especially significant when creating 3D tissue scaffolds where many functionally-identical copies of a particular sample may be required, especially in HTS operations where repeatability is paramount. Even in operations

that print acellular scaffolds, such as those meant for implantation or regenerative medicine purposes, process time minimization is highly beneficial, as this allows for scalable and extensible processes. Using this high throughput 3D bioprinter (HT-3DP), we showcase system capability by presenting a variety of different 3D-printed spatial geometries and control over biomaterial mechanical properties. Additionally, we demonstrate direct in-well 3D bioprinting and culturing of biomimetic human hepatocellular carcinoma scaffolds, as well as an example of drug screening utility with a functional drug response validation test of a commonly-used chemotherapy drug, and finally an example of dual-tissue printing capability. This work represents the first DLPbased 3D bioprinter capable of truly high throughput production of 3D tissue scaffolds of user-defined size, complexity, cell source, and tunable mechanical properties. A platform of this kind can be utilized to quickly and consistently produce custom tissue scaffolds on a high-volume scale and may accelerate discovery in such domains as pharmacological lead screening, disease modeling, and drug testing.

2. Results

2.1. Design and performance of the HT-3DP system

The core of the HT-3DP system shown in figure 1(A)is the digital micromirror device (DMD, Texas Instruments), which has an array of approximately four million (2560 × 1600) individually-addressable micromirrors—these micromirrors can pitch at defined angles to selectively reflect incident light, such that adjusting the total array of micromirrors enables dynamic reproduction of any input 2D image. Supporting technologies for the HT-3DP system include: a visible light source in the form of a 405 nm light emitting diode (LED) for photopolymerization; projection optics for projecting the DMD-reflected light; a 3-axis motorized stage with a well plate holder; and finally a computer with custom software for coordinating all hardware components. Together, these allow dynamic flexibility and reproducibility of printing parameters.

The 3D-printing workflow is as follows: the desired 3D construct is designed in computer-aided design (CAD) software and then digitally 'sliced' into a series of individual 2D cross-sectional images, which are then uploaded into the DMD. These designs may come from patient-derived medical imaging data, e.g. magnetic resonance imaging (MRI) or computed tomography (CT) scanning, thus enabling close approximation of a desired tissue type, or alternatively be user-defined custom geometries. The light source is then used to illuminate the DMD's micromirror array, the resultant reflection creating a 2D plane of spatially-modulated light that then dynamically changes as the image sequence displays. The reflected light pattern is projected via optics

through a hollow guidance probe, which by virtue of the 3-axis stage can descend into any given well of a well plate, which can be prefilled as needed with photosensitive prepolymer solution. The guidance probe's structure terminates with an optically clear glass window coated with polydimethylsiloxane (PDMS) to prevent adhesion of the polymerized construct. For a given prepolymer solution formulation, final feature sizes are dependent on the terminal projected pattern—each pixel of the projected image is reflected by an individual micromirror on the DMD (around 7.6 μ m in size), which when combined with select focusing optics, condenses the final image down to the microscale. The final resolution of the printed construct is dependent on a number of factors, including but not limited to: the optical setup used to focus the reflected image from the DMD onto the prepolymer solution, i.e. lense choice, aberrations, etc; material-induced light absorption and/or scattering, and free radical diffusion into areas outside photoexcited areas. The guidance probe starts submerged and nearly flush with the bottom of the well, and selective photopolymerization of the solution trapped between the probe's surface and the bottom of the well occurs based on the pattern of incident light. With the guidance probe held stationary relative to the well plate, synchronization between the projected light pattern and the movement of the 3-axis motorized stage enables continuous photopolymerization of the solution, thus resulting in a 3D construct (figure 1(B)) fabricated directly in any given well. Repetition and/or changing of print instructions can then occur across any arbitrary number of wells in the well plate. A photograph of the active build area can be seen in figure 1(C), where the guidance probe is shown in the midground above a 96-well plate suspended on the 3-axis motorized stage. For a given prepolymer hydrogel solution, total fabrication time is limited only by individual scaffold printing time and the time required to reposition the well plate for subsequent prints. Depending on the complexity of the printing structure, the total fabrication time for a fully-populated 96 well plate typically ranges from 20 to 40 min.

We chose to utilize poly(ethylene glycol) diacrylate (PEGDA) and gelatin methacryloyl (GelMA)-based materials as exemplars of the synthetic and biologically-derived materials commonly used in tissue engineering, but in principle any material capable of undergoing photopolymerization would be compatible with the HT-3DP. This affords flexibility across a number of user-defined choices, such as selection of scaffolding material and cell type, or desired biological and mechanical properties. Our system is particularly well-suited for biological applications, as the use of a 405 nm LED visible light source to photopolymerize aqueous, biologically-derived solutions eliminates any potential concerns regarding UV-radiation damage to living cells.

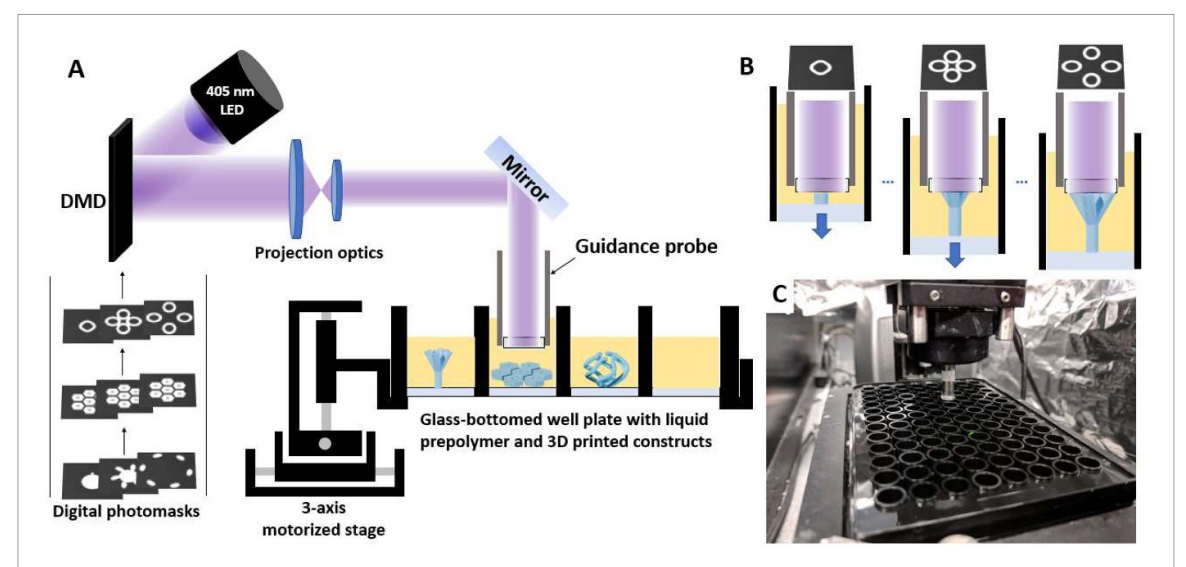


Figure 1. HT-3DP system. (A) Schematic depiction of high throughput 3D bioprinter (HT-3DP). Digital photomasks uploaded to a digital micromirror device (DMD) modulate projected light striking photosensitive prepolymer solutions held in a well plate on a 3-axis motorized stage. Computer-assisted synchronization of the light source, DMD pattern, and motorized stage enables rapid, continuous 3D printing on a high throughput scale. (B) Schematic time lapse depiction of HT-3DP's rapid continuous 3D-printing of a single construct. As time moves forward, projected digital photomasks advance synchronously with controlled downward stage motion, enabling fast production of 3D constructs. (C) Photograph of HT-3DP setup performing prints on a standard 96-well plate; probe shown in midground above the multiwell plate.

3. 3D-printing of biologically-relevant architectures

To establish HT-3DP fabrication capability, we 3D-printed exploratory architectures that employ a variety of different geometries and controllable parameters, using a PEGDA-based hydrogel. Figure 2 shows representative images of the various structures created, including (1) hollow bifurcations and complex tubes (figures 2(A-i), (A-ii), (B)), (2) smooth concave surfaces (figure 2(C-i)), (3) overhanging structures (figures 2(D-i,ii)), (4) sharp features under 10 microns in size (figure 2(E)), and (5) concentric rings that also demonstrate control over hydrogel mechanical stiffness (figures 2(F-i,ii)). These shapes were chosen based as exemplars of features that may be found in biological reality, or features that would otherwise be challenging to produce using other 3D printing modalities—together they represent a wide dynamic range of the types of structural complexity, length scales, and feature sizes that might be encountered in generating tissue scaffolds.

3.1. Tunability of scaffold mechanical properties

Figures 2(F-i,ii) show our ability to control the mechanical properties of our scaffolds—free radical photopolymerization induces crosslinking in the target material, and by modulating factors such as base material composition, light intensity, and exposure time, we can tune the final mechanical properties of our tissue scaffolds by controlling the crosslinking density. Here, we held constant the constituent concentrations of one of our prepolymer solutions at 7.5% GelMA and 0.6% lithium phenyl-2,4,6-trimethylbenzoylphosphinate (LAP), as well as

the intensity of the incident light at 16.7 mW cm^{-2} . Then, in a single print session that utilized a fivepart image sequence comprised of concentric rings surrounding a circle, we varied the exposure time such that each separate part of the construct received a different exposure time, and evaluated the effects of exposure time on elastic modulus (figure 2(F-i)). Starting from the innermost ring and moving outwards, each ring received successively longer exposure times in 10 s increments, with the innermost ring starting at 15 s and the final ring receiving 55 s. As can be seen from figure 2(F-ii), we see that this linear increase in exposure time produces a similarly linear trend in elastic modulus, ranging from 1.03 ± 0.57 kPa at the softest to 9.60 ± 1.22 kPa at the stiffest—this allows for the ability to precisely modulate mechanical stiffness in the same scaffold in one single print. These results represent testing for a single variation of prepolymer hydrogel but are easily extensible to other formulations depending on the desired mechanical properties.

3.2. High throughput production and consistent reproducibility of printed scaffolds

The HT-3DP's 3-axis motion stage is designed to accept commercially-available standardized well plates (typical dimensions 127 mm \times 83 mm). With its current optics and guidance probe tooling, the system can accommodate well plate densities of up to 96-wells, allowing rapid 3D-printing of any user-defined scaffold across any arbitrary number of wells. As an example, utilizing a 24-well plate, we printed a tubular conduit approximately 2.5 mm in outer diameter and 3 mm in height with an individual print time of 10 s per well. Printing 24

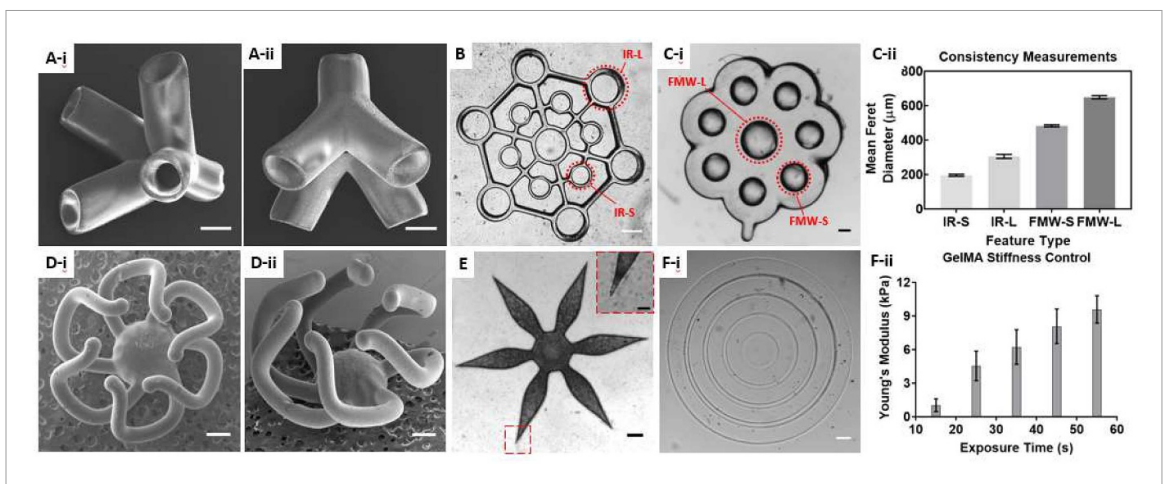


Figure 2. Various HT-3DP printed geometries. (A-i,ii) SEM images of a bifurcated hollow tube; scale bar = $500 \mu m$. (B) Brightfield top-down image of hollow tubes and interconnected struts; scale bars = $200 \mu m$. (C-i) Flower-like microwells with smooth concavities; scale bar = $200 \mu m$. (C-ii) Quantitative plot showing the feature size precision for selected representative features across two 3D-printed constructs. Interlocking rings—small (IR-S, N = 18) and Interlocking rings—large (IR-L, N = 21) from figure (b); Flower microwells—small (FMW-S; N = 42) and flower microwells—large (FMW-L; N = 6) from figure (C-i). Error bars are presented as standard deviations. (D-i,ii) SEM images of parallel spirals construct; scale bar = $500 \mu m$. (E) Brightfield image of star-shaped construct; scale bar = $200 \mu m$; inset shows sharp small feature <10 μm ; inset scale bar = $50 \mu m$. (F-i) Brightfield image of concentric GelMA rings printed with varying exposure times. Innermost dot received 15 s of exposure time and outermost ring received 55 s, with increments of 10 s; note increasing definition of ring borders from inner-to-outer; scale bar = $200 \mu m$. (F-ii) Quantitative plot showing relationship between compressive modulus and printing exposure time one day after printing. Error bars are standard deviation; N = 8 for all data points.

copies of such a construct takes approximately just 16 min (supplementary video 1 (available online at stacks.iop.org/BF/13/025007/mmedia)); scaling the same construct up to a 96-well plate would result in a total fabrication time of just under 40 min (supplementary video 2). By leveraging the standardization and consistency of well plate technology in conjunction with the speed afforded by our automated, micro-continuous projection printing method, we can dramatically improve our ability to 3D-bioprint structures on higher throughput scales.

We also evaluated the HT-3DP's ability to print scaffolds in terms of fabrication consistency, by having it print the same types of scaffolds multiple times in a row, and then comparing the measurements of select key features. Figure 2(C-ii) shows the mean Feret diameters of four circular features in two of the exploratory architectures—figure 2(B) shows a series of hollow tubes connected via struts, dubbed 'interlocking rings' (IR), and figure 2(C-i) shows a flower-like microwell (FMW) series. In the interlocking rings (IR) structure, we measured the Feret diameters of both the small (IR-S) and large (IR-L) hollow cylinders present in the structure, and similarly in the flower-like microwell (FMW) structure we measured the Feret diameters of the small (FMW-S) and large (FMW-L) microwells. As can be seen from figure 2(C-ii), each feature's standard deviation is small with respect to the original feature, with the lowest and highest standard deviations recorded as \pm 5.82 μ m for the IR-S and \pm 11.71 μ m for the IR-L, respectively (2.98% and 3.83% of the original feature sizes, for N = 18 and N = 21, respectively). We conducted an additional test of print precision

using a 96-well plate, fabricating acellular copies of a hexagonal scaffold biomimetically-inspired by liver lobule tissue in the four corner extremes of the plate (figure 3(A)). These locations were chosen as exemplar positions after the system was calibrated to ensure any loaded multiwell plates were coplanar with the build probe at any arbitrary position. Quantitative measurements were taken of three physical features of scaffold and evaluated for precision: the center hole diameter (CHD), the vertex-to-vertex length (V2 V) of one edge in the center hexagon, and the top-tobottom length (T2B) of the vertical chord in the center hexagon (3B). As can be seen in figure 3(D), we evaluated printing precision in a manner similar to that of figure 2(C-ii), where the standard deviation is small with respect to the feature size: the smallest and largest standard deviations recorded were \pm 1.71 μ m for the CHD and \pm 4.4 μm for the T2B, respectively (1.19% and 0.52% of the original feature size, for N = 42 and N = 6, respectively).

4. 3D-bioprinting HepG2 tissue scaffolds and functional testing against doxorubicin

To establish the HT-3DP's live cell printing capability, we utilized a well-established hepatocellular carcinoma cell line (HepG2) in 3D-printing biomimetic liver-inspired tissue scaffolds, whose shape and dimensions were chosen to mimic native hepatic lobule structure [10]. The liver carries out many critical functions related to metabolism, with any dysfunction closely tied to both disease- and drug-related pathologies [11]—thus HepG2 s serve as a suitable

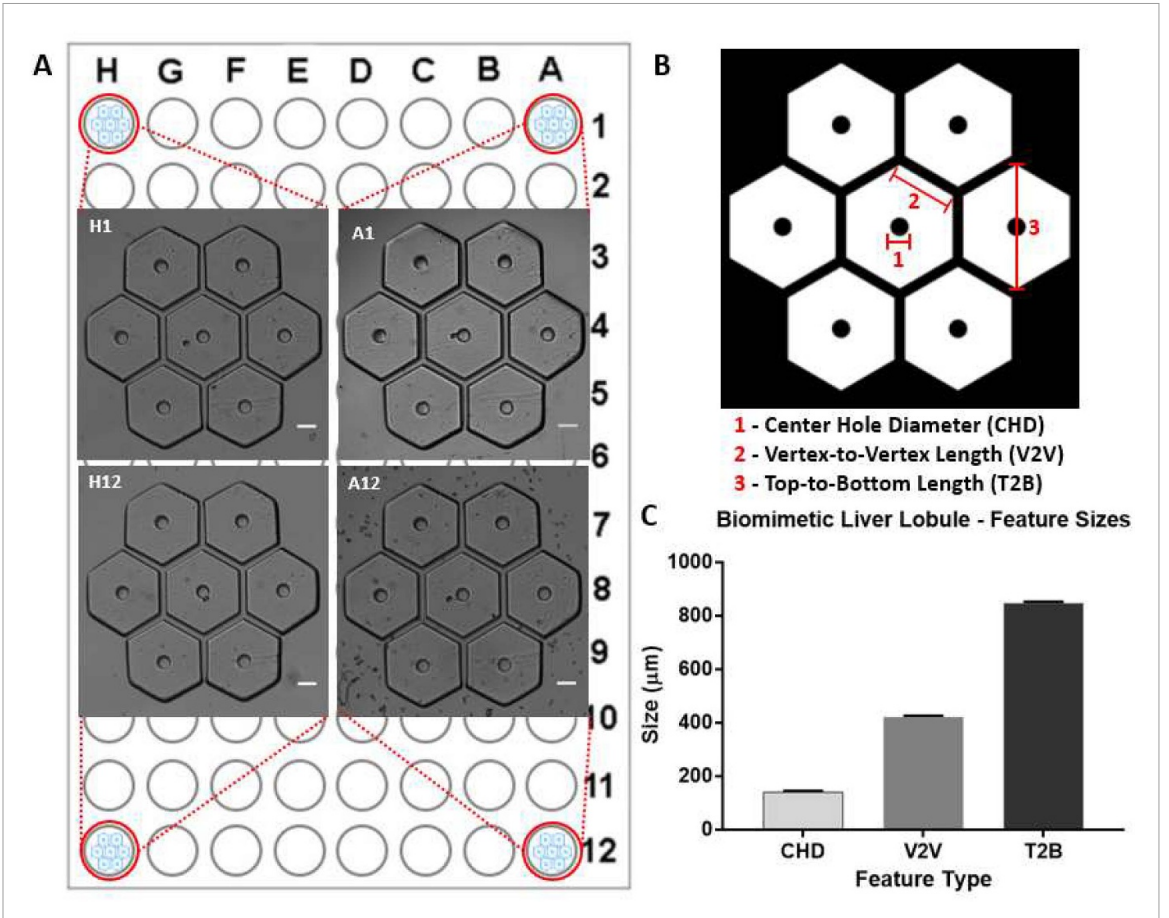


Figure 3. 96-well extremes consistency check. (A) Schematic depicting the locations of the four extremes of a 96-well plate where the HT-3DP printed. Insets: Brightfield images of acellular 3D-printed biomimetic liver lobule scaffolds printed at the four extremes depicted in the background. Scale bars = 200 μ m. (C) Quantitative plot depicting consistency of size measurements of the features shown in figure (B). CHD = 'Center Hole Diameter' (N = 4); V2V = 'Vertex to Vertex Length' (N = 24); T2B = 'Top to Bottom Length' (N = 4). Data represented as means, with error bars representing standard deviation.

model cell line for testing tissue scaffold fabrication techniques. A 7.5% (wt/vol) GelMA hydrogel solution was used, with print parameters chosen such that the final polymerized matrix stiffness was similar to that of native liver tissue. An acellular version was printed first to verify shape accuracy (figure 4(A)). Following verification, HepG2 cells were mixed with the GelMA hydrogel solution at a final concentration of 3 million cells per ml, and then printed using the HT-3DP as previously described, thus creating a 3D-printed tissue model of hepatocellular carcinoma (figure 4(B)). Live and dead cells were characterized by calcein AM and ethidium homodimer-I staining and imaged over the course of one week (figure 4(C)). Live/dead quantification (figure 4(D)) revealed that the majority of the cell population (>85%) were live cells at the end of one week, thus suggesting that the tissue scaffold was highly viable.

Having established HepG2 tissue viability, we next explored the functional utility of the 3D-bioprinted constructs, by conducting a simple well plate drug screening assay (figure 5(A)), which we deemed a suitable stand-in for any arbitrary drug screening assay capable of being conducted in a well plate. We chose the well-established chemotherapy

drug doxorubicin, which is commonly used to treat a number of oncological targets including liver-related issues in clinical patients, as well as in in vitro testing of human cell lines including HepG2 [12]. 3Dprinted HepG2 constructs were exposed to varying concentrations of doxorubicin, from 0 μ m to 100 μ m, and cell viability was evaluated at 24 and 48 hr time points afterwards (n = 3 per concentration, per time point, for a total of 42 samples). After the designated time points, a commerciallyavailable cell viability kit (CellTiterGlo 3D) was used to assess relative cell viability, in which the amount of fluorescently-labeled intracellular ATP is used as a quantitative indicator of metabolically active (thus live) cells. Considering doxorubicin's use as a chemotherapy drug, we thus expected and subsequently observed a decrease in viable HepG2 cells as we increased the doxorubicin concentration and/or exposure time. Brightfield images of treated HepG2 scaffolds (figure 5(B)) show how with increasing drug concentration, cell morphology visibly changes from the large, slightly translucent appearance of healthy cells to the shriveled, dark, and opaque characteristics of dead cells. This qualitative appearance is consistent with the quantitative data

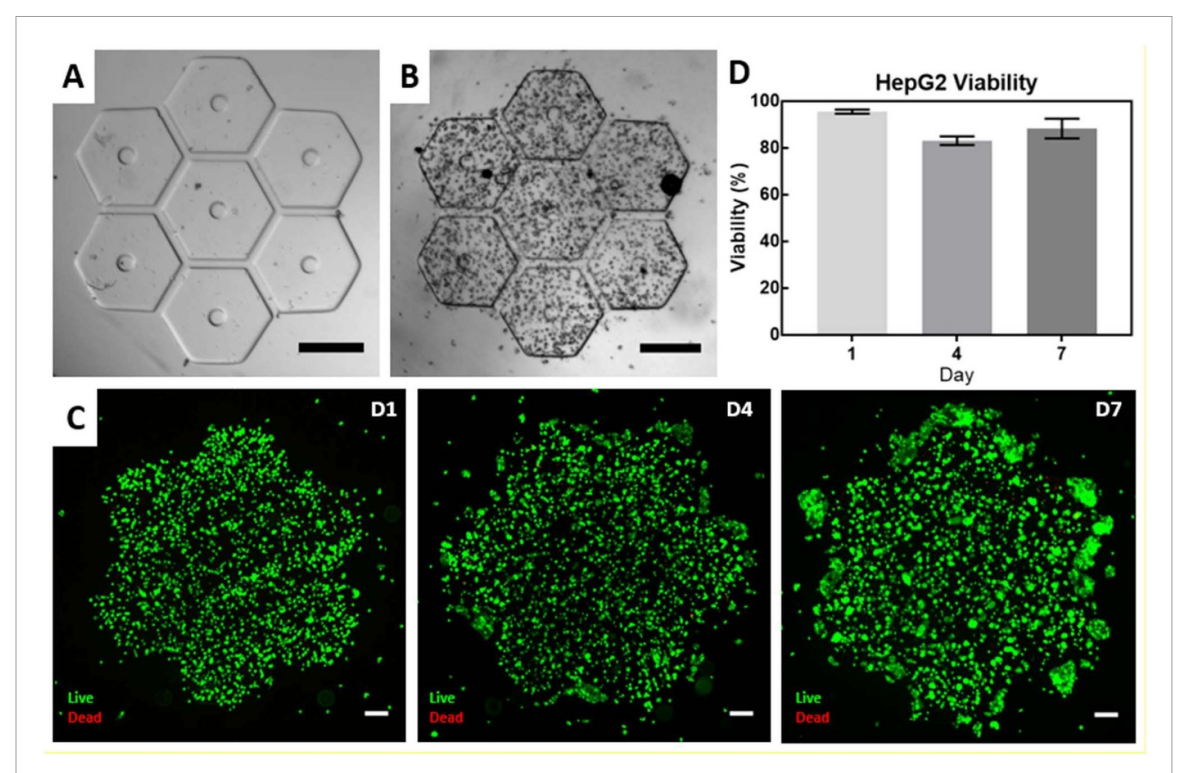


Figure 4. 3D bioprinted cancerous tissues \pm Live/Dead. (A) Brightfield image of an acellular 3D-printed scaffold, biomimetically patterned after liver tissue; scale bar = $500 \, \mu m$. (B) Brightfield image of a HepG2-cellularized 3D-bioprinted scaffold; scale bar = $500 \, \mu m$. (C) Representative fluorescent images showing Live/DeadTM staining of HepG2-cellularized 3D-bioprinted scaffolds over 1, 4, and 7 d respectively; scale bars = $200 \, \mu m$. (D) Quantitative plot depicting HepG2 cell viability over the course of 7 d; viability remains >85% at day 7. Data represented as means, with error bars as standard deviation. N = 3 for all data points.

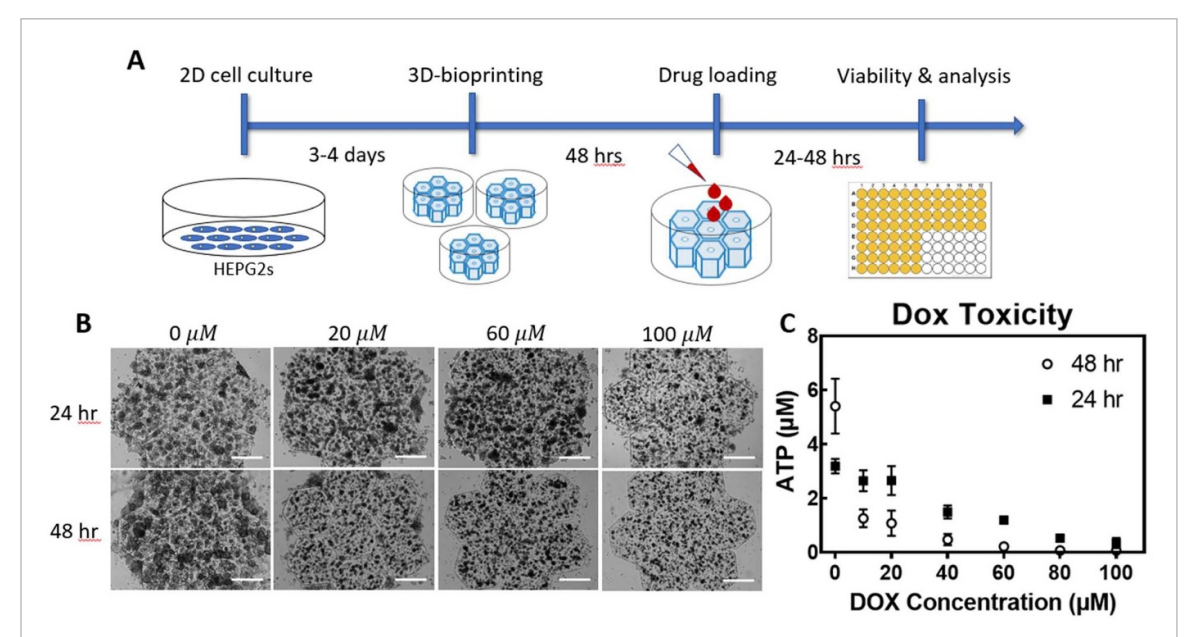


Figure 5. Doxorubicin viability testing of 3D bioprinted cancerous tissues. (A) Schematic depiction of the process timeline, starting from culturing and 3D-printing to drug loading and viability analysis. (B) Representative brightfield images of HepG2 scaffolds at varying doxorubicin concentrations and time points; scale bars = $500 \ \mu m$. (C) Quantitative plot depicting results of CellTiterGlo-3D viability assay, where a decreasing trend in ATP concentration occurs as doxorubicin concentration and exposure time increases. Data represented as means, with error bars as standard deviation.

(figure 5(C)), where a 2-way ANOVA was run on data from the 42 tissue scaffolds to compare the effect of doxorubicin concentration and exposure time on output ATP concentration. A significant effect of

exposure time (p < 0.0001), doxorubicin concentration (p < 0.0001), and an interaction between exposure time and doxorubicin concentration (p < 0.0001) was found. Therefore, ATP levels (thus cell viability)

can be easily controlled using both exposure time and/or doxorubicin concentration, confirming our expectations regarding the use of chemotherapeutic drugs on cancerous cells.

4.1. Dual cell-type population 3D-bioprinting

While we demonstrated the feasibility and utility of a HepG2-based tissue scaffold, it is composed of a single cell type. There is significant interest in tissue scaffolds incorporating multiple cell types, as these may better simulate the natural complexity of native tissues—interactions between multiple cell types may play crucial roles in various stages of development for both maturation and pathology-related domains [9]. To demonstrate the HT-3DP's capability in this regard, we fabricated dual-type tissue scaffolds (figure 6) comprised of: HepG2 cells for their liver-specific drug response, and human umbilical vein endothelial cells (HUVECs) for their well-documented vasculature-forming behavior [13] and potential interaction with fetal liver tissue [14].

Similar to the procedure used to print the HepG2only tissue scaffolds, a 7.5% (wt/vol) GelMA, 0.6% LAP hydrogel solution was used as the carrier solution for the cell populations. HUVECs and HepG2 s were grown using best 2D tissue culture practices, and subsequently incorporated into their own individual GelMA carrier solutions. With print parameters again chosen such that the final polymerized matrix stiffnesses were similar to that of their representative native tissue, the HUVEC-encapsulated GelMA was first printed in situ in the well plate to generate a 3D vasculature network, using a projection pattern 'inverted' from that of the HepG2 pattern (figures 6(A), (B)). After carefully flushing and removing the unreacted material, HepG2-encapsulated GelMA was input into the same well where the HUVEC-encapsulated print resided, and subsequently 3D-printed into the previously-used liver lobule shape (figures 6(C), (D)). Our control over the well plate's movement ensures close spatial coordinate registration, as can be seen in the spatial proximity of the two different tissue types even across two stages of printing (figure 6(E)).

5. Discussion and outlook

In recent years 3D-bioprinting technology has advanced greatly, with a widely-varying selection of modalities, from extrusion-based to light-based techniques [15]. Extrusion-based 3D bioprinters have previously shown promise in structured dispensing of hydrogel biomaterials and/or cells to create novel and functional tissue models of varying types [16, 17], but invariably have resolution and throughput limitations due to extrusion aperture constraints and their serialized approach to 3D-printing, respectively [18]. Certain types of light-based 3D bioprinters, such as 3D-stereolithography (SLA) systems, can circumvent

the physical limitations of nozzle extrusion by directly tracing lines of photopolymerization of aqueous hydrogels, yet are still hampered by the nature of serial printing, as 'line-by-line scanning' is inherently slower than 'layer-by-layer' [15]. Digital light processing (DLP)-based systems can further overcome the limitations of serial-type light-based 3Dprinters by projecting entire 2D planes of light in a layer-by-layer fashion, which can significantly lower the total fabrication time due to the elimination of serial scanning processes [19]. Indeed, DLP-based 3D bioprinters have demonstrated the ability to produce sophisticated 3D tissue scaffolds across a range of different tissue types, including vasculature [16, 20], cardiac tissue [21], skeletal muscle [22], hepatic tissue [10, 23], and the nervous system [24].

Recently, further DLP-based advancements have been shown, including the use of grayscale for functional grading [25], construct layer continuity [26], and even transitioning from layer-to-layer to volumetric-style printing [27–29]. While such techniques are able to print complex structures of varying length scales quickly, and indeed offer improved resolution and printing speed compared to their extrusion-based counterparts, these tend to be limited to 'single-vat' prints, not compatible with HTS which is often conducted in a multiwell plate. In HTS, large numbers of easy-to-use, consistent, and functional samples are required for ensuring accurate assays and evaluations; existing systems capable of high throughput printing of biological constructs tend to sacrifice 3D sophistication in favor of speed [30-32]. Thus, there is an unmet need for a 3Dbioprinting system capable of fabricating complex tissues, with an emphasis on high throughput scale.

Our HT-3DP system combines micro-continuous projection printing with automated well plate registration to quickly and scalably generate 3D tissue constructs at high throughput scales, thus overcoming limitations that other 3D bioprinters may have. With this technique, we were able to quickly produce 3D biomimetic HepG2 scaffolds for a functional drug response assay in the same well plate they were printed in, with minimal post-print processing. The materials used in printing are biocompatible, quickly photopolymerizable, and tunable for both feature resolution and mechanical properties. While this setup necessarily requires the use of photocrosslinkable materials, this technology is not solely limited to those—other naturally-derived materials yet non photocrosslinkable materials such as collagen, Matrigel, fibrin gels, or even animal-derived decellularized extracellular matrices [23, 33] can be included in composite formulations with a photopolymerizable material such as GelMA as the carrier component, so as to confer their biologically-beneficial properties to the final product.

The HT-3DP's enabling of direct encapsulation of chosen cell types with biocompatiable materials

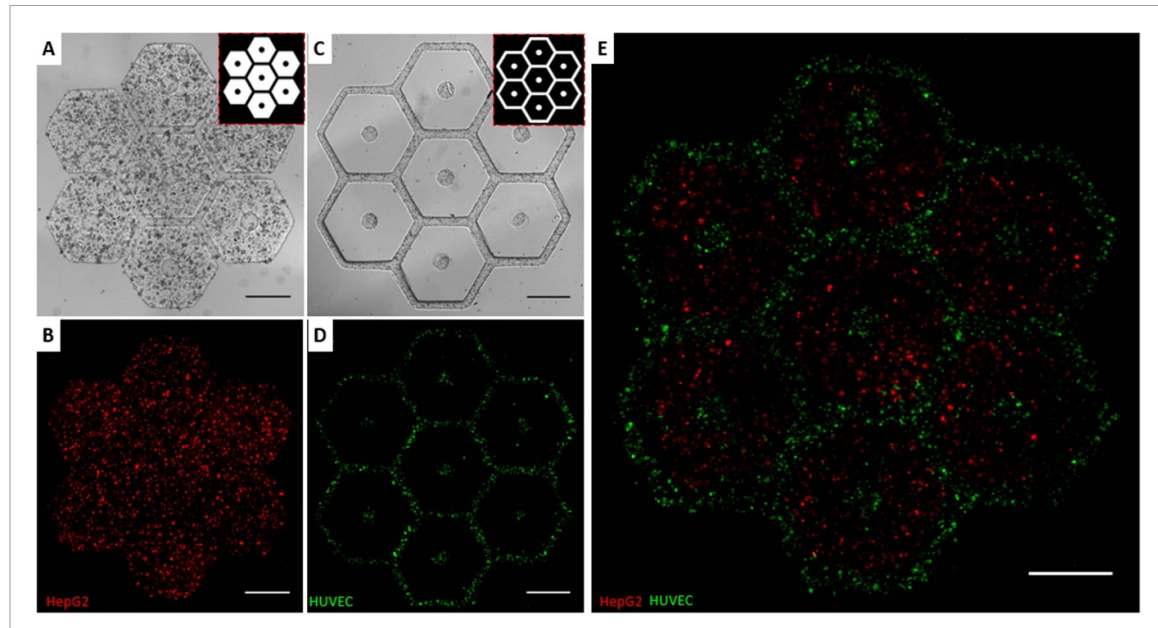


Figure 6. Dual cell population 3D-bioprinting of HepG2 s and HUVECs: (A) Brightfield image of a HepG2-only tissue scaffold; inset: projected image pattern. (B) Fluorescence image of a HepG2-only tissue scaffold. (C) Brightfield image of a HUVEC-only tissue scaffold, colored red via RFP-transfection; inset: projected image pattern. (D) Fluorescence image of a HUVEC-only tissue scaffold, colored green via CellTrackerTM-Green. (E) Fluorescence image of a combined HepG2 and HUVEC tissue scaffold. Scale bars = $500 \ \mu m$.

enables facile creation of 3D tissue models with immediate utility. While we chose a cellular density of 3 million cells per ml to mitigate light scattering issues and to better showcase the structural features of our tissue scaffolds, previous works utilizing similar light-based 3D printing have successfully printed tissue scaffolds with cell densities as high as 40 million cells per ml [10]. The dose- and time-dependent doxorubicin toxicity of our 3D-printed HepG2 scaffolds are comparable with previous reports using similar drug concentrations [34]. Additionally, the tested dosages of doxorubicin fall within the ranges commonly used in therapeutic settings, and the extremes mimic those of other studies that perform similar doxorubicin dosage testing [34, 35]. The doxorubicin assay, while simple in concept, is both extensible and scalable to potentially any in vitro drug screening assay that can be conducted in a well plate, underscoring the utility of the HT-3DP's ability to produce 3D tissue constructs on a high throughput scale. Furthermore, we show that the HT-3DP can print even more complex tissues by printing more than one cell type within the same construct, by printing the same HepG2 scaffold surrounded by a biomimetic vasculature network comprised of encapsulated HUVEC cells. This technique demsontrates how the HT-3DP can expand its application to creating models or pathologies that affect more than one tissue domain.

In summary, we present a 3D-bioprinting platform, capable of rapid, continuous 3D printing of constructs for drug screening purposes on a high throughput scale. We demonstrate capability in fabrication of small feature sizes (<10 microns), consistent reproduction of complex shapes, as well as mechanical property control over tissue scaffold stiffness. Our HT-3DP system combines microcontinuous projection printing with automated well plate printing to quickly and scalably generate functionally-identical 3D tissue models in standard well plates, enabling in situ well plate-based assays of functional drug response of human-type tissues. Future work in this domain may include enhancing the parallelization of fabrication, for even higher throughput scaffold production. Compared to lowervolume throughput 3D bioprinters, we anticipate that platforms such as our HT-3DP would create a new paradigm for drug and small molecule discovery, because high throughput combinatorial-screening investigations can potentially be conducted against 3D human-type tissue models instead of 2D monolayer cultures or non-human animal models, thus greatly increasing the efficiency of the drug discovery process.

6. Experimental methods

6.1. 3D construct build materials

Poly(ethylene) glycol diacrylate (PEGDA, $M_n=700\,$ Da) was purchased from Millipore-Sigma (USA). Gelatin methacryloyl (GelMA) was synthesized as described previously [33]. Photoinitiator lithium phenyl-2,4,6-trimethylbenzoylphosphinate (LAP) was synthesized in-house as described previously [36]. Photoinitiator Irgacure 819 was purchased from BASF.

The printing solution used for demonstrating controllable spatial architectures (figures 2(A)–(E))

was a hydrogel solution based on PEGDA. The solution was prepared as follows: 50% v/v PEGDA-700 as the prepolymer component, 1% wt/wt Irgacure 819 (BASF) as the photoinitiator, and 5% v/v yellow food dye (Wilton) as a visible light absorber for increasing spatial resolution, all in 1x Dulbecco's phosphatebuffered saline (DPBS) as the solvent. The printing solution used for demonstrating mechanical stiffness control and for the HepG2-encapsulated scaffolds was prepared by mixing GelMA at 7.5% wt/vol and LAP at 0.6% wt/vol in 1x DPBS. The printing solution used for printing the HepG2-encapsulated tissue scaffolds was prepared by mixing a solution of 15% wt/vol GelMA and 1.2% LAP wt/vol at a 1:1 ratio with a HepG2 cell suspension at a concentration of 6 million cells ml^{-1} , for a final solution of 7.5% wt/vol GelMA, 0.6% LAP, and 3 million HepG2 cells ml^{-1} . The printing solution used for printing the HUVECencapsulated tissue scaffolds was prepared by mixing a solution of 15% wt/vol GelMA and 1.2% LAP wt/vol at a 1:1 ratio with a HUVEC cell suspension at a concentration of 6 million cells ml⁻¹, for a final solution of 7.5% wt/vol GelMA, 0.6% LAP, and 3 million $HUVECs ml^{-1}$.

6.2. High throughput 3D printer (HT-3DP)

All 3D-printed constructs shown in this work were printed via the described HT-3DP setup. The DMD chip utilized in the HT-3DP setup is the DLP® LightCrafterTM 9000 Evaluation Module (Texas Instruments), and has a 2560 × 1600 micromirror array. Constructs were digitally designed in CAD software (Autodesk, AutoCAD), with the resulting 3D models in .STL format sliced with in-house MAT-LAB script into a series of digital photomasks. Photomask series were digitally-uploaded to the DMD, with individual photomask display synchronized to digitally-controlled motion of a 3-axis motorized stage (Zaber) while under controlled illumination from a 405 nm visible light LED. Synchronization of all hardware components was coordinated with a computer running in-house software (Visual Studio).

Briefly, the printing process is as follows: a defined volume of prepolymer solution is dispensed into a target well in a methacrylated [37] well plate placed on a controllable 3-axis motorized stage. Then, the well plate is maneuvered such that by way of relative positioning, the HT-3DP's printing probe is submerged in the target well, with the probe's bottom surface flush with the well's floor (or a methacrylated glass coverslip laid in said well, if necessary). A thin coating of polydimethylsiloxane (PDMS) adhered to the bottom of the probe head creates a non-stick surfacecombined with the prepolymers' acrylate chemistry, this enables in-progress 3D constructs to preferentially stick to the targeted methacrylated well bottom, as well as ensuring long-term stable attachment during tissue culturing. At the start of printing, software coordinates the hardware components such that light source activation, DMD photomask sequence, and stage motion are synchronized—as the projected light pattern selectively photopolymerizes a volume of prepolymer solution, the stage (and thus the well plate) can move down relative to the probe's position, allowing fresh solution to move into the vacated space and be polymerized in turn. The stage motion can also be set to stationary, allowing the user to photopolymerize a static layer of prepolymer solution if desired. With full control over the stage's motion, the probe head itself can also be used to pre-agitate the liquid prepolymer in any given well, in the event of significant cell settling due to gravity over long time scales. In this way, the HT-3DP can rapidly and continuously print 3D constructs, as the combination of the projection of an entire 2D plane of light and controllable stage motion allows significant reduction in fabrication time compared to serially-printing extrusionbased printers.

6.3. Mechanical stiffness control

Concentric GelMA rings of varying stiffnesses showcased in figure 2(F) were fabricated with our HT-3DP setup as previously described. The build material utilized GelMA, and was prepared as follows: 7.5% wt/vol GelMA as the prepolymer component, 0.6% wt/vol LAP as the photoinitiator, all in 1x Dulbecco's phosphate-buffered saline (DPBS) as the solvent. A five photomask series was used, starting with a 500 μ m diameter circle in the center, followed by four nested rings of increasing diameter; the outermost ring has a diameter of 3.5 mm, and each ring has a lateral thickness of 250 μ m. The innermost dot received 15 s of 405 nm light exposure time, and going outwards, each subsequent ring received an additional 10 s of exposure time, for a final exposure time of 55 s for the outermost ring.

6.4. Liver-biomimetic and vasculature-biomimetic tissue scaffolds

The hexagonal liver-biomimetic scaffolds $(2.4 \text{ mm} \times 2.4 \text{ mm} \times 250 \mu\text{m})$, both acellular and cell-laden versions, were fabricated with our HT-3DP setup as previously described. A liver-biomimetic design was used to create the photomask series. The vasculature-biomimetic scaffolds shown in the dual cell population prints were similarly patterned and fabricated. The build material used for these prints was GelMA—acellular versions used 7.5% wt/vol GelMA + 0.6% wt/vol LAP solution as previously described, and the cell-laden versions used the same, with the addition of the respective cell type at a final concentration of 3 million HepG2 s or HUVECs cells ml⁻¹. HepG2 (human hepatocellular carcinoma, ATCC) and HUVEC (human umbilical vein endothelial cell, ATCC) were cultured using standard 2D cell culture best practices. HepG2 cells were maintained in Dulbecco's modified eagle medium (DMEM, Gibco) supplemented with 10% fetal bovine serum (FBS), 1% PenStrep, and 0.2% Normacin. HUVECs were maintained in Endothelial Cell Growth Medium-2 (EGMTM-2, Lonza) supplemented with EGMTM-2 SingleQuotsTM supplements). Before bioprinting, HepG2 or HUVEC cells were digested via 0.05% trypsin-EDTA and gently mixed with pre-prepared GelMA/LAP hydrogel prepolymer for a final solution consisting of 7.5% wt/vol GelMA, 0.6% LAP, and 3 million cells ml⁻¹ density. Fluorescence in the dual cell population prints was achieved via Red Fluorescent Protein (RFP)-trasnfection of the HepG2 s (shown in red) and CellTrackerTM-Green (ThermoFisher Scientific) staining of the HUVECs.

6.5. Micro-mechanical testing

GelMA hydrogels used for the hepatocellular carcinoma scaffolds were measured for their bulk elastic modulus via micro-scale compression testing on the commercially-available platform 'Microsquisher' (CellScale), with results gathered through the included software (SquisherJoy). Briefly, the system operates by means of a piezoelectric actuator moving a cantilever of defined stiffness against a target sample—this cantilever compresses the sample while in view of a high-resolution camera. By comparing on-screen cantilever displacement with force data measured during compression, the elastic modulus can be calculated from the linear region of the generated stress-strain curve, which was done by in-house MATLAB scripts. Cylindrical samples (D = 500 μ m, $H = 250 \mu m$, N = 6 per exposure time) matching the exposure times of the individual concentric rings construct were compressed at 10% strain with a 2 μ m s⁻¹ strain rate after overnight acclimation in a room temperature 1x DPBS bath.

6.6. Image acquisition and processing

Scanning electron microscopy (SEM) images of both the 'bifurcated tube' and 'parallel spirals' constructs were prepared as follows: a cleaning soaking session in 100% isopropyl alcohol (IPA), followed by air-drying at room temperature for 24 h, then sputtercoating with iridium for 7 s, followed by imaging using a Zeiss Sigma 500 scanning electron microscope. Brightfield and fluorescence images of all other 3D-printed constructs were acquired with a Leica DMI 6000B microscope (Leica Microsystems), with 2.5x or 5x objectives and included tile-and-stitch software. Photographs and video of HT-3DP infrastructure taken via consumer DSLR and smartphone cameras. FIJI/ImageJ (National Institutes of Health) was used to collect measurements for feature size comparison and consistency check data.

6.7. Quantification of feature sizes in 3D-printed constructs

Brightfield images of 3D-constructs were taken via light microscopy (Leica) at 5x magnification and processed in image analysis software FIJI/ImageJ (NIH). For measurements made for ellipsoidal regions of interest, minimum and maximum Feret diameters were obtained for each region of interest via manual fitting of the oval-shaped measuring tool. Data reported as mean \pm standard deviation, where the mean was calculated as the square root of the product of the minimum and maximum Feret diameter. For edge length and otherwise non-ellipsoidal regions of interest, measurements were obtained via the line measuring tool, and data reported as mean \pm standard deviation.

6.8. Statistical analysis

Data points on all graphs represent mean values, with error bars representing standard deviation where stated. Visual inspection of box-and-whisker plots revealed normally distributed data with no significant outliers. A 2-way analysis of variance (ANOVA) with replication was conducted on doxorubicin toxicity data. All statistical analysis and associated graphical output was done using Excel (Microsoft) or Graph-Pad Prism (GraphPad).

6.9. Quantification of cell viability in Live/Dead® assay

A cell viability assay kit (LIVE/DEAD^(R) Viability/Cytotoxicity Kit, Invitrogen) was used to assess cell viability for the constructs on Days 1, 3, and 7 post-printing. Briefly, the tissue constructs (n = 3 for each time point) were washed with 1x DPBS after removing the culture medium, after which they were stained with a solution comprised of 2 μ m calcein AM (live cell stain) and 4 μ m ethidium homodimer-1 (dead cell stain) in DPBS. After incubating at 37 °C for 30 min, fluorescent and bright field images of the constructs were taken with a Leica DMI 6000B microscope (2.5x Objective, Leica Microsystems). Live/dead cells were counted manually in FIJI/ImageJ (NIH) in blinded experiments for each sample, with data reported as mean \pm standard deviation.

6.10. Quantification of cell viability in doxorubicin exposure and CellTiter-Glo(R) luminescent assay

Liver tissue constructs (2.4 mm \times 2.4 mm \times 250 μ m) were printed with 7.5% GelMA + 0.6% LAP, encapsulating 3 million ml⁻¹ HEPG2 cells, and were allowed to grow. At Day 3 post-fabrication, the constructs were exposed to varying concentrations of doxorubicin {0, 10, 20, 40, 80, and 100 μ m, N = 4 for each concentration}, for two different time points {24 and 48 h, N = 4 for each time point}. Doxorubicin solution preparation was as follows: powdered drug was resuspended in DMSO to a stock concentration of 80 mm. An aliquot was taken and further diluted to 10 mm, upon which 0, 2, 4, 8, 16, and 20 μ l were added to separately prepared aliquots of 2 mls prepared cell culture media to make

0, 10, 20, 40, 80, and 100 μ m doxorubicin solutions, respectively. The cell constructs in the well plates were aspirated of any existing media, and were then loaded with the doxorubicin-laced media. After 24 h of doxorubicin exposure, a CellTiter-Glo® luminescent cell viability assay kit was used as recommended to assess the cell viability of the constructs post-doxorubicin exposure. The assay indirectly determines cell viability by quantitating the amount of ATP present, an indicator of metabolically active cells. After the requisite amount of drug exposure, the first step of the CellTiter-Glo® assay was performed, where a cell lysis reagent was added to wells containing the cell-laden scaffolds, thus lysing any cells present and releasing intercellular ATP content into the surrounding solution. Afterwards, a secondary reagent was added that luminesces on interaction with ATP—the strength of the luminescence is quantifiable by means of a luminescence plate reader (Infinite 200 PRO, Tecan, Mannedorf, Schweiz), and is directly proportional to the amount of ATP present in the solution. By comparing the luminescence values of our samples against a co-prepared standard curve, we can establish a relative assessment of cell viability.

Acknowledgments

The authors would also like to thank Dr David Berry for mentoring and advice. This work was supported in part by grants from the National Institutes of Health (R01EB021857, R21AR074763, R21HD100132, R33HD090662) and National Science Foundation (1903933, 1937653).

Competing interests

The authors declare no competing interests.

Author contributions

H H, S Y, W Z and S C conceived and initiated this project. H H, S Y, and X M designed and performed the experiments, as well as analyzed experimental outputs. L K, G V, N L, X W, and H S contributed to sample fabrication, processing, data gathering, and analysis. H H, S Y, X M, W Z, and S C wrote the manuscript. S C supervised the project.

Data availability

The data that support the findings of this study may be made available from the authors on reasonable request. All requests for materials and data will be reviewed by the Office of Innovation and Commercialization—University of California San Diego to verify whether the request is subject to any intellectual property or confidentiality obligations.

Any materials and data that can be shared will be released via a Material Transfer Agreement.

Materials and correspondence

Materials and correspondence may be directed to Shaochen Chen, PhD.

ORCID iD

Henry H Hwang https://orcid.org/0000-0001-6690-2929

References

- Hughes J P, Rees S S, Kalindjian S B and Philpott K L 2011 Principles of early drug discovery *Br. J. Pharmacol*. 162 1239–49
- [2] Avorn J 2015 The \$2.6 billion pill—methodologic and policy considerations N. Engl. J. Med. 372 1877—9
- [3] Giacomotto J and Ségalat L 2010 High-throughput screening and small animal models, where are we? Br. J. Pharmacol. 160 204–16
- [4] Musther H, Olivares-Morales A, Hatley O J D, Liu B and Rostami Hodjegan A 2014 Animal versus human oral drug bioavailability: do they correlate? *Eur. J. Pharm. Sci.* 57 280–91
- [5] Langhans S A 2018 Three-dimensional in vitro cell culture models in drug discovery and drug repositioning *Front*. *Pharmacol.* 9
- [6] Bhadriraju K and Chen C S 2002 Engineering cellular microenvironments to improve cell-based drug testing *Drug Discov. Today* 7 612–20
- [7] Verjans E-T, Doijen J, Luyten W, Landuyt B and Schoofs L 2018 Three-dimensional cell culture models for anticancer drug screening: worth the effort? *J. Cell. Physiol.* 233 2993–3003
- [8] Yildirimer L et al 2019 Engineering three-dimensional microenvironments towards in vitro disease models of the central nervous system Biofabrication 11 032003
- [9] Edmondson R, Broglie J J, Adcock A F and Yang L 2014 Three-dimensional cell culture systems and their applications in drug discovery and cell-based biosensors ASSAY Drug Dev. Technol. 12 207–18
- [10] Ma X et al 2016 Deterministically patterned biomimetic human iPSC-derived hepatic model via rapid 3D bioprinting Proc. Natl. Acad. Sci. 113 2206–11
- [11] Kaplowitz N 2005 Idiosyncratic drug hepatotoxicity Nat. Rev. Drug Discov. 4 489–99
- [12] Buschauer S, Koch A, Wiggermann P, Müller M and Hellerbrand C 2018 Hepatocellular carcinoma cells surviving doxorubicin treatment exhibit increased migratory potential and resistance to doxorubicin re-treatment in vitro Oncol. Lett. 15 4635–40
- [13] Takebe T et al 2014 Generation of a vascularized and functional human liver from an iPSC-derived organ bud transplant Nat. Protoc. 9 396–409
- [14] Si-Tayeb K, Lemaigre F P and Duncan S A 2010 Organogenesis and Development of the Liver *Dev. Cell* 18 175–89
- [15] Hwang H H, Zhu W, Victorine G, Lawrence N and Chen S 2017 3D-printing of functional biomedical microdevices via light- and extrusion-based approaches *Small Methods* 2 1700277
- [16] Kolesky D B et al 2014 3D bioprinting of vascularized, heterogeneous cell-laden tissue constructs Adv. Mater. 26 3124–30
- [17] Kang H W et al 2016 A 3D bioprinting system to produce human-scale tissue constructs with structural integrity Nat. Biotechnol. 34 312–19

- [18] Zhu W et al 2018 Rapid continuous 3D printing of customizable peripheral nerve guidance conduits Mater. Today (https://doi.org/10.1016/j.mattod.2018.04.001)
- [19] Zhang A P et al 2012 Rapid fabrication of complex 3D extracellular microenvironments by dynamic optical projection stereolithography Adv. Mater. 24 4266–70
- [20] Zhu W *et al* 2017 Direct 3D bioprinting of prevascularized tissue constructs with complex microarchitecture *Biomaterials* 124 106–15
- [21] Ma X et al 2019 3D-printed micro-scale force gauge arrays to improve human cardiac tissue maturation and enable high throughput drug testing Acta Biomater. 95 319–27
- [22] Kim J H et al 2018 3D bioprinted human skeletal muscle constructs for muscle function restoration Sci. Rep. 8 12307
- [23] Ma X et al 2018 Rapid 3D bioprinting of decellularized extracellular matrix with regionally varied mechanical properties and biomimetic microarchitecture Biomaterials 185 310–21
- [24] Koffler J et al 2019 Biomimetic 3D-printed scaffolds for spinal cord injury repair Nat. Med. 1 263–9
- [25] Kuang X et al Grayscale digital light processing 3D printing for highly functionally graded materials Science Advances 5 eaav5790 (available at: https://advances.sciencemag. org/content/5/5/eaav5790)
- [26] Tumbleston J R et al 2015 Continuous liquid interface production of 3D objects Science 347 1349–52
- [27] Beer M P D et al 2019 Rapid, continuous additive manufacturing by volumetric polymerization inhibition patterning Sci. Adv. 5 eaau8723

- [28] Kelly B E et al 2019 Volumetric additive manufacturing via tomographic reconstruction Science 363 1075–9
- [29] Shusteff M et al 2017 One-step volumetric additive manufacturing of complex polymer structures Sci. Adv. 3 eaao5496
- [30] Rodríguez-Dévora J I, Zhang B, Reyna D, Shi Z and Xu T 2012 High throughput miniature drug-screening platform using bioprinting technology *Biofabrication* 4 035001
- [31] Xu F et al 2011 A three-dimensional in vitro ovarian cancer coculture model using a high-throughput cell patterning platform Biotechnol. J. 6 204–12
- [32] Guillemot F et al 2010 High-throughput laser printing of cells and biomaterials for tissue engineering Acta Biomater. 6 2494–500
- [33] Yu C et al 2019 Scanningless and continuous 3D bioprinting of human tissues with decellularized extracellular matrix Biomaterials 194 1–13
- [34] Ye N, Qin J, Liu X, Shi W and Lin B 2007 Characterizing doxorubicin-induced apoptosis in HepG2 cells using an integrated microfluidic device *Electrophoresis* 28 1146–53
- [35] Lupertz R, Watjen W, Kahl R and Chovolou Y 2010 Doseand time-dependent effects of doxorubicin on cytotoxicity, cell cycle and apoptotic cell death in human colon cancer cells *Toxicology* 271 115–21
- [36] Liu J et al 2019 Rapid 3D bioprinting of in vitro cardiac tissue models using human embryonic stem cell-derived cardiomyocytes Bioprinting 13 e00040
- [37] Soman P, Chung P H, Zhang A P and Chen S 2013 Digital microfabrication of user-defined 3D microstructures in cell-laden hydrogels *Biotechnol. Bioeng.* 110 3038–47